Autonomous Calibration of Non-Contact Power Monitors

Andre Aboulian, John S. Donnal, *Member, IEEE*, and Steven B. Leeb, *Fellow, IEEE*

***Abstract*— Non-contact power monitors use electromagnetic field sensors to measure voltage and current in multiphase power lines without any ohmic contact or geometric isolation of the conductors. The complex field geometry requires these sensors to be calibrated before use. Existing work has focused on manual calibration procedures requiring a service interruption, additional loads, or other intrusive techniques. This paper introduces an autonomous calibration technique that can be used to bootstrap additional non-contact power monitors from an existing power monitor located elsewhere in the distribution network. This provides the flexibility to "zoom-in" with downstream monitors or "zoom-out" with upstream monitors and efficiently target the loads of interest. Laboratory benchmarks and installations on the U.S. Coast Guard and Naval vessels show that autonomous calibration is accurate and robust with non-contact monitors reading within 1% of commercial power meters.**

***Index Terms*— Magnetic sensors, calibration, monitoring, power systems, power measurement, inverse problems, non-intrusive load monitoring.**

I. Introduction

HIGH bandwidth power monitors can detect faults in mission-critical electromechanical equipment before they become failures reducing downtime and maintenance costs. Using non-intrusive load monitoring (NILM) algorithms a single power monitor at an upstream node (eg a circuit breaker or distribution panel) can disaggregate the power waveform into individual loads providing virtual submeters for each appliance [1]. Unfortunately, NILM systems have seen limited deployments in commercial and industrial settings. This is in part because traditional power monitors require ohmic contact with high voltage conductors making them expensive and inconvenient to install.

Non-contact power monitors (see Fig. 1) do not require ohmic contact or geometric isolation of conductors greatly reducing the installation cost. These systems work by measuring the electromagnetic field around the power line which is proportional to the current and voltage of the conductors. The close proximity of wires in the power line cause these fields to overlap spatially making it difficult to measure a particular field in isolation. Therefore, to produce accurate measurements, non-contact power monitors must be calibrated to the particular field geometry before use. Existing work has focused on manual calibration techniques that require a service interruption or addition of a known load to the power system [2]. In many industrial and commercial power systems this is not feasible as loads are hard wired to the power system and service interruptions are cost prohibitive.

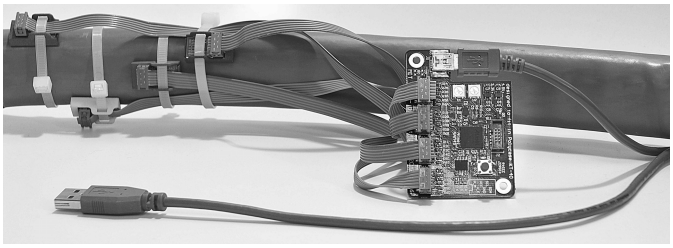

Fig. 1. Non-contact power monitor connected to a multi-phase power line. Non-contact monitors measure per-phase current and voltage using the electromagnetic fields outside the power line.

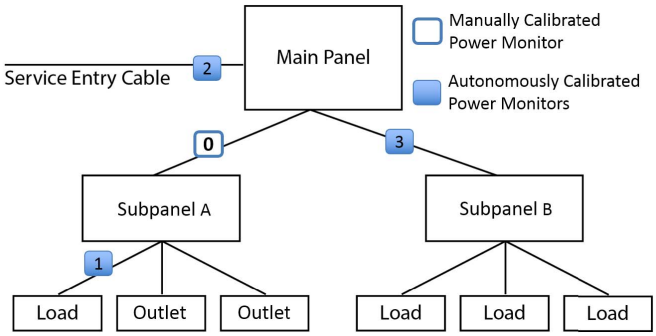

Fig. 2. Instrumenting a power distribution network with multiple non-contact monitors. The initial monitor (0) is manually calibrated. Monitors 1 and 2 are autonomously calibrated from 0. Monitor 3 is then autonomously calibrated from 2.

This paper introduces an autonomous bootstrap procedure that allows a non-contact monitor to self-calibrate using information from an existing upstream or downstream power monitor. This amortizes the installation cost of the "root" monitor across all of the child devices and provides a flexible power monitoring solution. As shown in Fig. 2, downstream monitors can be added for precise measurements of mission critical loads and upstream monitors can be added to provide facility-wide measurements or branch across to other distribution circuits.

The paper is organized as follows. Section II provides an overview of the field of non-intrusive load monitoring and

Manuscript received March 26, 2018; revised May 1, 2018; accepted May 6, 2018. Date of current version June 12, 2018. This work was supported in part by the Office of Naval Research NEPTUNE Program, in part by The Grainger Foundation, in part by the MIT-KUST Program, and in part by the Cooperative Agreement between the Masdar Institute of Science and Technology (Masdar Institute), Abu Dhabi, UAE, and the Massachusetts Institute of Technology, Cambridge, MA, USA under Grant 02/MI/MIT/CP/11/07633/GEN/G/00. The associate editor coordinating the review of this paper and approving it for publication was Dr. Ferran Reverter. *(Corresponding author: John S. Donnal.)*

A. Aboulian and S. B. Leeb are with the Massachusetts Institute of Technology, Cambridge, MA 02139 USA.

J. S. Donnal is with the U.S. Naval Academy, Annapolis, MD 21402 USA (e-mail: donnal@usna.edu).

Digital Object Identifier 10.1109/JSEN.2018.2837350

non-contact sensors in particular. Section III then presents the autonomous calibration procedure. Autonomous calibration uses organic transients in the power system to synchronize the child monitor to the parent. In modern power systems the presence of power converters, variable speed drives and other power electronics make it particularly difficult to isolate discrete transients. Section IV provides an algorithm for detecting suitable transients for autonomous calibration. Finally, Section V presents the results of laboratory benchmarks and deployments on a US Navy and US Coast Guard vessel. These results show that autonomously calibrated non-contact monitors are a practical and accurate power monitoring solution.

II. Non-Intrusive Load Monitoring

Monitoring electricity consumption can provide maintenance diagnostics, track human activity, and improve energy conservation [3]–[5]. Non-intrusive load monitors aim to deliver these results with minimal hardware infrastructure. NILM's rapidly sample the power waveform, often at multiple kilohertz, and identify individual loads by their characteristic transients [6]. A NILM installed at the main panel will theoretically provide visibility of every electronic load in a facility. However, disaggregating net power usage by individual loads is an area of active research and depends heavily on the number and types of loads in the facility [7]. While signal processing can be used to enhance the dynamic range of a NILM, it is sometimes, necessary to "zoom in" on a reduced subset of loads for higher resolution data or to eliminate transients produced by other equipment [8]. These limitations may not be apparent until after the monitor is installed.

A. Non-Contact Power Monitors

One of the main impediments to non-intrusive load monitoring is the cost and inconvenience of installing a mains power meter. Voltage sensors require galvanic contact and current sensors require geometric isolation of each conductor. While these sensors may be designed into new equipment, the cost to retrofit them into existing infrastructure may be prohibitively high or simply not possible if mission critical systems cannot be turned off. Non-contact power monitors simply attach to the outside of the power line and do not required a skilled technician or service interruption for installation. Because they are installed without knowledge of the electromagnetic field geometry the sensors must be calibrated before they can produce accurate measurements.

B. Current Calibration

The magnetic fields generated by currents within a multi-conductor cable superimpose linearly according to Ampere's Law. Individual phase currents can be recovered from the magnetic field measurements with a linear transformation. Each current I_n contributes to the sensed magnetic field B_m by a factor $K_{m,n}$. Equation (1) explicitly relates three independent currents to a vector of measurements from M magnetic field sensors, for example. The matrix entries can be determined experimentally through a calibration process.

$$\begin{bmatrix} B_1 \\ B_2 \\ \vdots \\ B_M \end{bmatrix} = \begin{bmatrix} K_{1,1} & K_{1,2} & K_{1,3} \\ K_{2,1} & K_{2,2} & K_{2,3} \\ \vdots & \vdots & \vdots \\ K_{M,1} & K_{M,2} & K_{M,3} \end{bmatrix} \times \begin{bmatrix} I_A \\ I_B \\ I_C \end{bmatrix} \tag{1}$$

The *current matrix* $\mathbf{K}$ describes how the currents combine to produce magnetic fields. Its pseudo-inverse $\mathbf{K}^+$, specifies how the magnetic fields combine to produce currents. Equation (2) shows how phase currents are calculated from magnetic field measurements.

$$\vec{I} = \mathbf{K}^+ \vec{B} \tag{2}$$

A calibration process is any method that determines the $\mathbf{K}$ matrix. This could be achieved by measuring the isolated effect of each current on each magnetic field sensor. For instance, a simple but impractical calibration strategy might be to pass a known constant current through only one conductor at a time. In terms of equation (1), the currents would be fixed at $I_A = I_{cal}$ and $I_B = I_C = 0$ while measuring the $\vec{B}$ response. Although this would successfully determine the first column of $\mathbf{K}$, it would be unrealistic to demand that some phase currents are zero.

The calibration method discussed in [2] also requires introducing a known load on each phase. However, this method operates on current transients rather than absolute levels, which allows the power system to operate normally during calibration. A *calibration transient* occurs every time a known test load turns on or off, causing a change in current level. Equation (1) can be rewritten as $\partial\vec{B} = \mathbf{K}\partial\vec{I}$. Similar to before, $\partial I_A = I_{cal}$ and $\partial I_B = \partial I_C = 0$ while $\partial\vec{B}$ is measured. Since $\vec{I}$ and $\vec{B}$ are linearly related, the $\mathbf{K}$ matrix can also be determined from changes in these quantities. The calibration is cycled at an fixed frequency so it can be extracted from background transients using a Fourier Transform.

C. Voltage Calibration

The electric fields generated by voltages in a multi-conductor cable superimpose linearly and may be monitored capacitively using techniques discussed in [9]–[11]. Assuming a well regulated utility with balanced voltages, the electric field at any point around the cable is a phase shifted sinusoid at the utility frequency. The angular difference between the sensor measurement E and a particular phase can be calculated using the transient of a unity power factor calibration load. If the calibration load draws only real power, then the angular difference between the phase current and E is exactly the angular difference between E and the phase voltage. Once the angular difference of each phase is calculated ($\psi_{A,B,C}$), the voltages can be reconstructed from a single electric field sensor:

$$\begin{bmatrix} V_A \\ V_B \\ V_C \end{bmatrix} = E \times \frac{A_{\mathrm{rms}}}{\mathrm{RMS}(E)} \times \begin{bmatrix} e^{-j\psi_A} \\ e^{-j\psi_B} \\ e^{-j\psi_C} \end{bmatrix} \tag{3}$$

where $A_{\mathtt{rms}}$ is the nominal line voltage. The geometry of the electric field is complex and generally contains multiple nodes or areas of low signal. It is often advantageous to attach multiple sensors around the cable and determine the most reliable sensor (by amplitude) during the calibration process. After calibration, unused sensors may be physically removed or deactivated.

III. Autonomous Calibration Algorithm

Manual calibration requires the addition of a load that is sized and switched to introduce observable, precisely timed, current transients. Other loads that are either very large or change frequently may distort these transients and corrupt the computed current matrix and voltage angles. A more significant limitation may be the installer's ability to energize the calibration load at all. The electrical network in Fig. 2 demonstrates the problem. The calibration load is connected to an outlet. The only outlets are on Subpanel A which means Meter 1 and 3 cannot be calibrated. Meter 2 on the main panel is unlikely to calibrate well because the combined current of the hardwired loads is likely much greater than the current that can be drawn by an outlet. This situation is common in commercial and industrial environments and has been documented in NILM installations aboard USCG Cutters [12].

Autonomous calibration does not require a test load. The calibrator-induced transients are replaced with organic transients that are observed by both a calibrated parent and an uncalibrated child. The parent monitor may be upstream or downstream of the child. In Fig. 2, Monitor 0 is the parent of both Monitor 1 and 2. Once Monitor 2 is calibrated it can be used as a parent for Monitor 3. In this way a network of power monitors may be bootstrapped from a single calibrated installation. The autonomous calibration algorithm uses the parent's current and voltage data (I, V) and the child's electromagnetic field data (E, B), to determine the child's current matrix $\mathbf{K}$ and voltage angles $\psi_{A,B,C}$. Line numbers in the sections below refer Alg. 1.

A. Preprocessing Data

The parent and child data sets are AC waveforms at the utility line frequency. To simplify transient detection these signals are reduced to DC harmonic envelops using the Sinefit algorithm [13] (lines $1-5$). Sinefit computes the in-phase ($\mathcal{I}$) and quadrature ($\mathcal{Q}$) envelopes of an AC signal against a reference sinusoid. The result, called PREP, is a complex signal $\boldsymbol{Y} = \mathcal{I}_{\boldsymbol{Y}} + j \cdot \mathcal{Q}_{\boldsymbol{Y}}$. The real and imaginary parts correspond to in-phase and quadrature harmonic components, respectively. The magnitude $\mid \boldsymbol{Y} \mid$ and angle $\angle \boldsymbol{Y}$ can be used to describe the signal in polar form. The parent's PREP is computed using I in reference to the associated V. The child's PREP is computed using B in reference to the electric field sensor E. If multiple electric field sensors are available, the sensor with the largest RMS response is used. In the PREP streams load transients become DC steps as shown in Fig. 3. The PREP stream for the parent's phase n is $\boldsymbol{C}_n$ and the PREP stream for the child's sensor m is $\boldsymbol{S}_m$.

Algorithm 1: Autonomous Calibration

Input: Parent's currents $\{I_1 .. I_N\}$ and voltages $\{V_1 .. V_N\}$. Child's magnetic $\{B_1 .. B_M\}$ and electric $\{E_1 .. E_M\}$ fields.

1: **for each** $n \in \{1..N\}$ **do** ▷ Compute PREP Streams
2: $\quad \boldsymbol{C}_n \leftarrow \textsc{Sinefit}(I_n, V_n)$
3: $E \leftarrow \textsc{MaxRMS}(\{E_1 .. E_M\})$
4: **for each** $m \in \{1..M\}$ **do**
5: $\quad \boldsymbol{S}_m \leftarrow \textsc{Sinefit}(B_m, E_{ref}))$
6: $\textsc{Align}(\{\boldsymbol{C}_1 .. \boldsymbol{C}_N\}, \{\boldsymbol{S}_1 .. \boldsymbol{S}_M\})$
7: **for each** $n \in \{1..N\}$ **do** ▷ Find Common Transients
8: $\quad \mathcal{D}(\boldsymbol{C}_n) \leftarrow \textsc{DetectTransients}(\boldsymbol{C}_n)$
9: **for each** $m \in \{1..M\}$ **do**
10: $\quad \mathcal{D}(\boldsymbol{S}_m) \leftarrow \textsc{DetectTransients}(\boldsymbol{S}_m)$
11: $\textsc{EliminateMultiPhase}(\{\mathcal{D}(\boldsymbol{C}_1) .. \mathcal{D}(\boldsymbol{C}_N)\})$
12: **for each** $n \in \{1..N\}$ **do**
13: $\quad$ **for each** $m \in \{1..M\}$ **do**
14: $\quad\quad T_{m,n} \leftarrow \textsc{MatchTransients}(\mathcal{D}(\boldsymbol{S}_m), \mathcal{D}(\boldsymbol{C}_n))$
15: **for each** $n \in \{1..N\}$ **do** ▷ Compute Calibration Factors
16: $\quad m\_\mathtt{mast} \leftarrow \textsc{SelMaster}(\{T_{1,n} .. T_{M,n}\})$
17: $\quad$ **for each** $m \in \{1..M\}$ **do**
18: $\quad\quad \mathtt{scale} \leftarrow \textsc{CalcScale}(T_{m,n})$
19: $\quad\quad \mathtt{sign} \leftarrow \textsc{CalcSign}\left(\angle\mathcal{D}\left(T_{m,n}\right), \angle\mathcal{D}\left(T_{m\_\mathtt{mast},n}\right)\right)$
20: $\quad\quad \mathbf{K}_{m,n} \leftarrow \mathtt{scale} \times \mathtt{sign}$
21: $\quad \psi_n \leftarrow \textsc{CalcAngle}\left(\angle\mathcal{D}\left(T_{m\_\mathtt{mast}, n}\right)\right)$

Output: Child's current matrix $\mathbf{K}$ and voltage angles $\{\psi_1 .. \psi_N\}$.

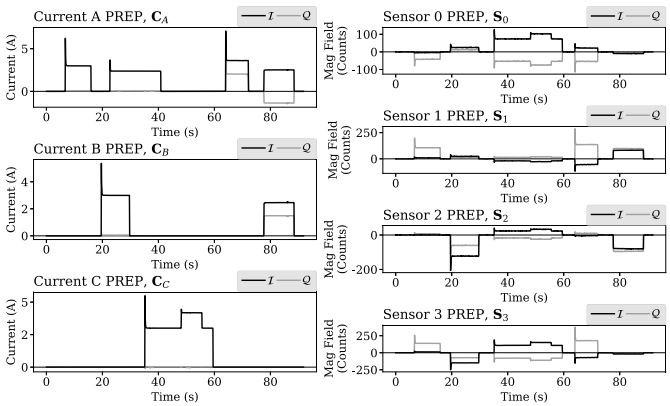

Fig. 3. Current PREP streams $\boldsymbol{C}_n$ (left) from the parent monitor and sensor PREP streams $\boldsymbol{S}_m$ (right) from the child monitor.

The parent and child monitors are sampled independently which often creates a time offset between the parent and child data. A cross-correlation is used between $\sum_{n=1}^{N} \Delta \boldsymbol{C}_n$ and $\sum_{m=1}^{M} \Delta \boldsymbol{S}_m$ to determine this offset. The Δ operator represents the discrete first-derivative function. The peak index in the cross correlation is the time offset between the streams. Shifting the child by this offset aligns the streams which is required for transient matching (line 6).

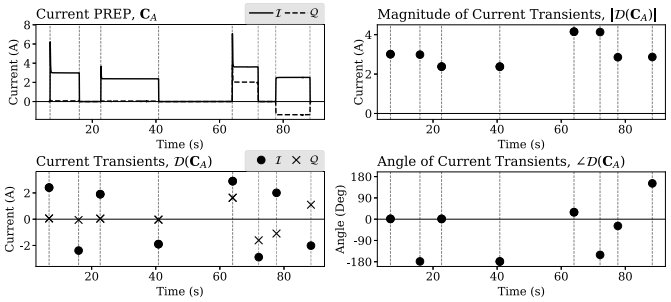

Fig. 4. Comparison of PREP data to its transient stream (left). Derived transient magnitudes and angles also shown (right).

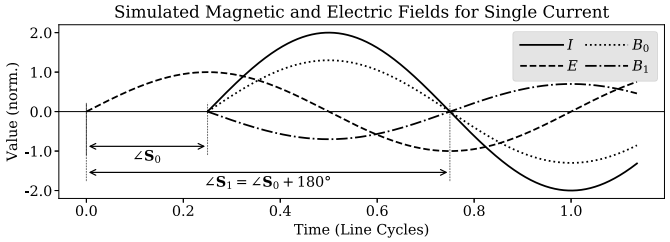

Fig. 5. Simulated non-contact sensor responses to a current I. The sign of the magnetic field (B_0, B_1) depends on the sensor's proximity to the I conductor versus the neutral conductor (see section III-E). The phase relationship between the measured electric field E and a particular conductor's voltage depends on the cable geometry (see section III-F).

B. Load Transients

Transients occur through the natural operation of equipment in the power system. These appear as DC changes in the PREP stream. Ideally the derivative of PREP is zero except for impulses at load transients. In practice the derivative is noisy because the power waveform is not a series of clean steps. A process for reliably detecting transients in PREP is described in Section IV. In this section, which overviews the entire calibration process, we assume that $\mathcal{D}(X)$ is the ideal stream of load transients.

When a load turns on or off it causes a change in the $\mathcal{I}$ and/or $\mathcal{Q}$ components of the PREP stream $\boldsymbol{Y}$. The corresponding transient stream $\mathcal{D}(\boldsymbol{Y}) = \mathcal{D}(\mathcal{I}_{\boldsymbol{Y}}) + j \cdot \mathcal{D}(\mathcal{Q}_{\boldsymbol{Y}})$ is also complex-valued. Transient streams are determined for all currents C and sensors S (lines $7-10$). The relationship between a PREP stream and its corresponding transient stream is illustrated in Fig. 4.

C. Eliminating Multi-Phase Loads

The calibration algorithm uses single phase transients to isolate the contribution of each current to each sensor response. Multiphase loads do not provide this isolation so they cannot be used for calibration. Three phase and line-line load transients are eliminated by removing any simultaneous transients in the $\mathcal{D}(C_n)$ streams (line 11).

D. Matching Transients

Only the subset of organic transients that are detected by both the parent and the child monitor are suitable for use in calibration. The matched transient dataset $T_{m,n}$ is the pair of transient streams $\mathcal{D}(\boldsymbol{C}_n)$ and $\mathcal{D}(\boldsymbol{S}_m)$ with all non-coincident transients removed (lines $12-14$). There are $N \times M$ such sets. Unmatched transients in $\mathcal{D}(\boldsymbol{C}_n)$ can occur when the parent is upstream of the child or when sensor m is not sensitive to the phase n field. Unmatched transients in $\mathcal{D}(\boldsymbol{S}_m)$ can occur when the child is upstream of the parent or when the sensor m is sensitive to other fields besides phase n.

E. Computing the Current Matrix

Each matched transient dataset corresponds to an element in the current matrix $\mathbf{K}$. The $\mathbf{K}_{m,n}$ coefficient is the ratio of transients in $T_{m,n}$. Each transient pair provides an estimate of this coefficient. Unfortunately the sign of $\frac{\mathcal{D}(\boldsymbol{S}_m)}{\mathcal{D}(\boldsymbol{C}_n)}$ depends on both the sensor alignment and the actual change in current. The sign ambiguity is differed until later by considering magnitudes only. A least squares regression is applied in a two-step process to determine the optimal $|\,\mathbf{K}_{m,n}\,|$ estimate (line 18). First, a fit is computed using all transient pairs in $T_{m,n}$. Even in a noise-free environment, there may be outliers to this fit line. For example, if a common load and an unrelated load in an upstream circuit are energized simultaneously, the downstream child would only detect the common load while the upstream parent would detect the sum of both loads leading to an incorrect transient ratio. Therefore, points deviating significantly from the initial fit line are eliminated. The linear regression is then recomputed for a tighter fit with the remaining transients.

The sign of $\mathbf{K}_{m,n}$ depends primarily on sensor m's proximity to the neutral conductor versus the phase n conductor. The neutral field is the inverse of the phase field which is why a traditional current sensor integrating the total flux around the wire bundle measures zero amperes. Because the wire geometry is not known the sign of the reconstructed current cannot be determined from magnetic field measurements alone. The is resolved by making the largest coefficient in each column positive and assigning the other coefficients mutually consistent signs. Incorrectly signed currents will be corrected by the voltage angle calculated later. The largest coefficient corresponds to the sensor with the strongest response to that particular phase. This sensor is called the master (line 16). The other coefficients in the column are signed by comparing the angle of sensor transients in the set $T_{m,n}$ with the master's in the set $T_{m\_\mathtt{mast},n}$ (line 19). If $\angle\mathcal{D}(\boldsymbol{S}_m) = \angle\mathcal{D}(\boldsymbol{S}_{m\_\mathtt{mast}})$ the coefficient is positive, if the angles are complements the coefficient is negative. Note the angular difference must be 0 or π because sensors measure either the phase or the neutral field as shown in Fig. 5. This completes the computation of current matrix $\mathbf{K}$.

F. Computing Voltage Angles

Manual calibration relies on a unity power factor test load. This means calibrator transients in $\angle\mathcal{D}(\boldsymbol{S}_m)$ are simply the voltage angle ψ_m (see section II-C). In automatic calibration the transients are generated by loads with varying power factors. The effect of these power factors is removed by subtracting $\angle\mathcal{D}(\boldsymbol{C}_n)$ from $\angle\mathcal{D}(\boldsymbol{S}_m)$ and averaging over the

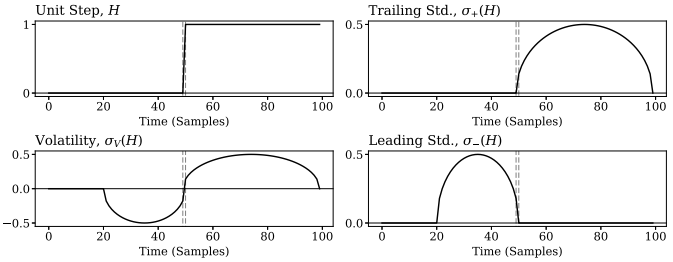

Fig. 6. Various standard deviation functions applied to the unit step.

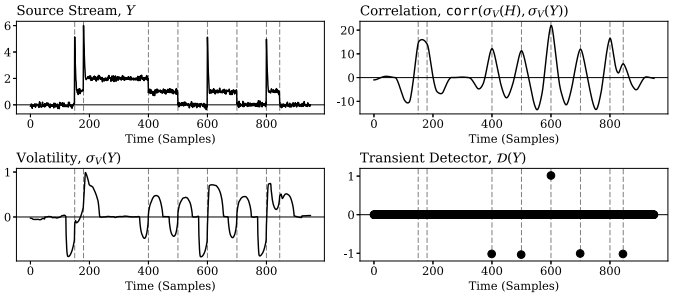

Fig. 7. Intermediate signals of the transient detector. Dotted vertical lines represent candidate transient locations.

transients. The difference is a combination of the voltage angle and a possible sign correction for the current.

$$\begin{aligned}\angle\mathcal{D}\left(\boldsymbol{C}_n\right) &= \theta_{\mathtt{pf}}\\ \angle\mathcal{D}\left(\boldsymbol{S}_m\right) &= \theta_{\mathtt{pf}} + \theta_{\mathtt{sign}} + \psi_m\\ \angle\mathcal{D}\left(\boldsymbol{S}_m\right) - \angle\mathcal{D}\left(\boldsymbol{C}_n\right) &= \theta = \theta_{\mathtt{sign}} + \psi_m \end{aligned} \tag{4}$$

The current matrix assumes the master sensor responds positively to the phase current. If this assumption is incorrect $\theta_{\mathtt{sign}} = \pi$, otherwise $\theta_{\mathtt{sign}} = 0$. That is, if $\mid \theta \mid > \pi$, the current's sign is incorrect. In this case the matrix K can be corrected, or if the PREP I/Q streams are the desired output (as is often the case) using θ as the voltage angle will compensate for the flipped current automatically (line 21). While any of the sensors may be used to calculate the voltage angle, the master sensor is preferred because it has the strongest response to the phase and therefore provides a numerically stable estimate.

IV. Load Transient Detector

Organic transients, unlike calibrator-induced transients are not precisely timed or sized. The autonomous calibration algorithm hinges on the ability to reliably detect these transients in experimental data. This section describes the transient detector function $\mathcal{D}$, which produces a stream containing a non-zero point at each load transient. These points are located at sudden changes, such as the inrush waveform. The value corresponds to the amount of change in the steady-state level due to the transient.

Typical edge detection strategies are unsuitable for autonomous calibration. Simple thresholding must be delicately tuned for each specific environment [14]. Frequency-based filtering or convolving edge profiles alleviates the threshold sensitivity, but these filters are selective to transient shapes. A second-derivative Gaussian kernel provides versatile detection and offers decent locality [15], [16] but introduces a time shift that distorts the transient alignment between streams.

For these reasons, autonomous calibration employs a custom transient detection algorithm. The transient detector $\mathcal{D}$ uses a windowed standard deviation (STD). The trailing function σ_+ outputs the STD of the preceding W_T samples, while the leading function σ_- targets the next W_L samples. When either of these functions moves over a significant change, the output gradually rises then falls. Figure 6 shows these functions applied to the unit step H, which is an ideal transient. These functions are largely useful because they return approximately zero over regions of constant-centered

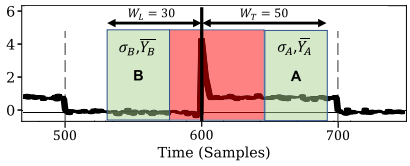

Fig. 8. The trailing and leading windows positioned at a candidate transient, shown against the input signal. The valid intervals (green) are analyzed on either side of the ignored samples (red).

fluctuations. The volatility function $\sigma_V = \sigma_+ - \sigma_-$ quantifies the difference in deviation before and after each point. Since H is steady on either side of the step change, the $\sigma_V(H)$ stream inflects at this point.

The transient detector calculates the volatility stream of the input data Y, which has been smoothed with a small median filter. The $\sigma_V(Y)$ stream takes on the appearance of $\sigma_V(H)$ near each transient. Cross-correlating these two volatility streams produces $R = \mathtt{corr}(\sigma_V(H), \sigma_V(Y))$, which peaks at each transient, as shown in Fig. 7. The relative extrema of R above an empirically-set threshold τ_{corr} become candidates locations for load transients. This threshold is specific to the type of input data (ex. currents) and establishes the minimum change that would be considered a valid transient. Since the STD function attenuates small fluctuations in the input signal, τ_{corr} does not vary greatly between environments.

The candidate transients must be verified against the input stream to ensure they correspond to acceptable changes. If a transient occurs within W_T before or within W_L after another transient, they are both discarded. Then, the samples on either side of the remaining transients are ignored, since they are likely to vary dramatically. The farther samples are used to ascertain steady-state properties. These regions are visually depicted in Fig. 8 relative to the window sizes used for the STD functions in previous steps. Notice these regions are asymmetrical, since the startup waveform may be unsteady for many line cycles.

The STD is computed over the valid regions before and after the transient, yielding σ_B and σ_A respectively. The difference $\sigma_{bal} = \mathtt{abs}(\sigma_A - \sigma_B)$ must be below a small threshold τ_{bal} to signify that the fluctuations are "balanced" on either side. If this check passes, then averages $\overline{Y}_A$ and $\overline{Y}_B$ are taken over the same regions. Their difference quantifies the steady-state change used in the output stream $\mathcal{D}(Y)$, which appears

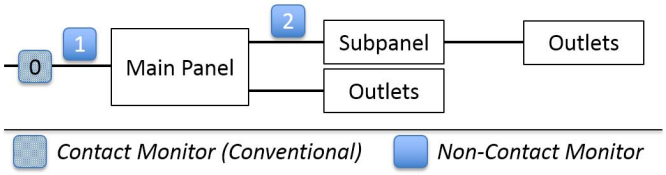

Fig. 9. Monitor configuration for calibration experiments. Monitor 0 is a conventional power monitor used to benchmark the calibration results. Monitors 1 and 2 are non-contact monitors. All combinations of parent-child calibrations are evaluated.

in Fig. 7. Notice that some candidate transients do not appear in this stream since they failed various verification checks.

Transient detection may be performed on one scalar stream at a time. For complex PREP streams, it is preferable to locate transient candidates on $|\ \boldsymbol{X}\ |$ rather than on the dependent $\mathcal{I}_{\boldsymbol{X}}$ and $\mathcal{Q}_{\boldsymbol{X}}$ components individually. This way, detection is not influenced by rotation. Verifying that $\sigma_{bal} < \tau_{bal}$ occurs on the components individually, although the candidate is discarded if the check fails for either. Finally, the steady-state change is computed for each component. This special handling of PREP streams ensures that when a transient appears on $\mathcal{D}(\mathcal{I}_{\boldsymbol{X}})$, it must also appear at the same location on $\mathcal{D}(\mathcal{Q}_{\boldsymbol{X}})$.

V. Experimental Results

The autonomous calibration algorithm has been tested in a laboratory setting. It has also been tested in field installations on the microgrids of U.S. Navy and U.S. Coast Guard vessels.

A. Lab Experiments

The autonomous calibration method was tested in a laboratory setting under various metering configurations and with a diverse set of loads on a three-phase 120/208 volt five-wire service. The resulting calibrations were assessed on the basis of accurate current reconstruction to evaluate the end-to-end success of algorithm and sensor hardware described in this paper. The electrical topology of the testbed is shown in Fig. 9. Non-contact meters monitor the main panel and the subpanel. The main panel is also monitored by a conventional meter to provide cross-validation. This meter uses LEM LF305-S and LEM LV25-P transducers to measure per-phase currents and voltages, respectively. These analog measurements are digitally sampled with a LabJack UE9 DAQ. In this setup, controlled loads can be introduced on either the main panel or the subpanel. Loads connected to the subpanel outlets appear on all monitors, while loads on the main panel outlets only appear on monitors 0 and 1. The complete experimental setup is shown in Fig. 10.

Various types of loads are introduced on each panel during the experiment shown in Fig. 11. Incandescent bulbs and high-power resistors are connected line-to-neutral as real-power loads. These are cycled on each phase of the subpanel, while similar loads are energized on the main panel ($t = [0, 80]$). Some transients occur on different phases, while others deliberately coincide on the same phase. Similarly, real-power loads

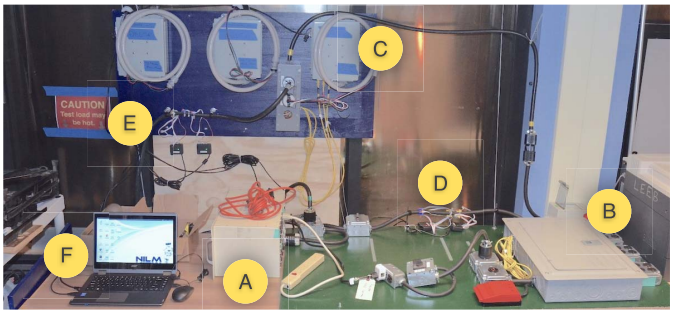

Fig. 10. The bench setup includes a main panel (A) and a subpanel (B). A conventional power meter (C) monitors the main panel. Non-contact meters are installed on the multi-conductor cables leading to the subpanel (D) and main panel (E). A commodity computer (F) runs the calibration utility and the NILM software infrastructure.

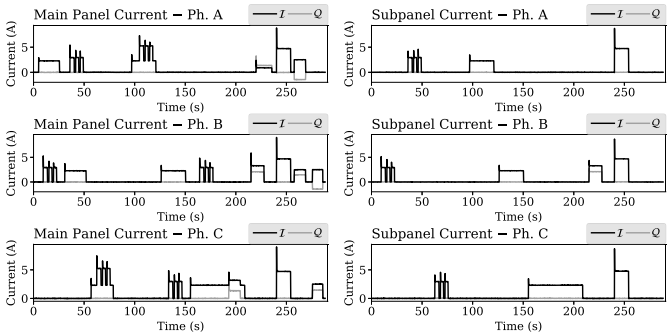

Fig. 11. Per-phase currents for the laboratory experiment, including the main panel (left) and subpanel (right).

TABLE I
Calibration Accuracy for the Laboratory Experiment

Monitors		Magnitude Err. [%]			Power Factor Err. [%]		
Parent	*Child*	*Min*	*Avg*	*Max*	*Min*	*Avg*	*Max*
Meter 0	Meter 1	0.01	0.46	1.35	0.00	0.10	0.45
Meter 0	Meter 2	0.02	0.34	0.89	0.00	0.05	0.34
Meter 1	Meter 2	0.00	0.37	1.47	0.00	0.03	0.60
Meter 2	Meter 1	0.01	0.38	0.93	0.00	0.02	0.44

are cycled on the main panel while others are energized on the subpanel ($t = [80, 180]$). A lamp dimmer is connected to various phases of both panels, since it exhibits a significant non-unity power factor ($t = [180, 240]$). Finally, some $3\varnothing$ and line-to-line loads are powered ($t = [240, 300]$).

Autonomous calibration was performed using all possible combinations of monitors. For instance, Monitor 1 on the main panel is manually calibrated and then used to autonomously calibrate the Monitor 2 on the subpanel, and vice versa. The results were checked for the relative accuracy of the autonomously calibrated monitor versus a reference monitor for each experiment.

Accuracy statistics for transient magnitude and power factor across all loads are presented in Table I. These experiments demonstrate the effectiveness of autonomous calibration. The low error rate for magnitude proves the algorithm correctly computes the current matrix $\mathbf{K}$. Similarly, the low power factor errors verifies that the voltage angles ψ are correctly determined. The loads were strategically chosen and simultaneously

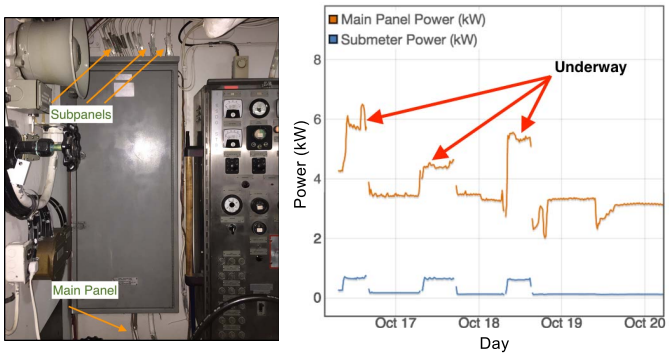

Fig. 12. Main distribution panel aboard a YP ship (left). Power data from the autonomously-calibrated subpanel, compared to the main panel (right). Power consumption increases on both panels during underway operation.

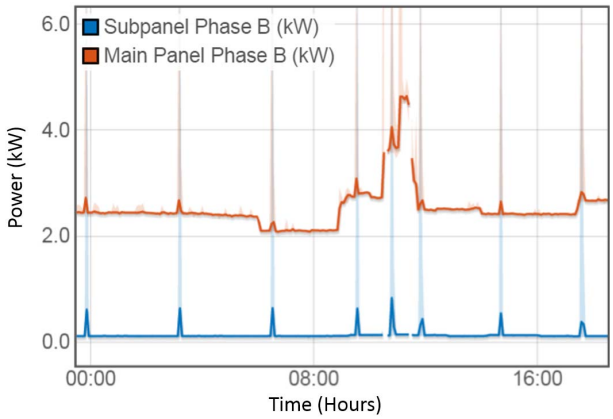

Fig. 13. Phase B power from the autonomously-calibrated auxiliary subpanel versus the main panel power. The radar produces pulse transients that are easier to detect on the subpanel. Only Phase B is shown for clarity although the radar draws power on both B and C phases.

energized to cover most foreseeable cases. Furthermore, the multiphase loads are ignored during calibration but considered while evaluating the accuracy of reconstructed currents.

B. Shipboard Application on a Navy Vessel

As a second test environment, non-intrusive power monitors were installed aboard a US Navy Yard Patrol (YP) vessel. This ship provides an ideal testing platform, as generation and consumption of electricity occurs within a closed microgrid aboard the ship. The electrical system is a radially distributed network centered around the main distribution panel shown in Fig. 12. The cable entering this panel is used to deliver energy from the generator at sea or from the utility at shore. A non-contact monitor is installed on this feeder and manually calibrated using a test load. The branch circuits serving various subpanels are instrumented with autonomously calibrated non-contact monitors.

The ship employs a 208V delta-connected electrical system. Autonomous calibration can be adapted to this system without any changes to the fundamental steps of the algorithm. Kirchoff's current law on a delta network implies that one of the three phase currents is a dependent variable, carrying the algebraic sum of the other two phase currents. Calibration is conducted with two sequential applications of a line-to-line load. For instance, a load is first energized between phases A and B; then, between C and B. In this case, phase B is analogous to the neutral current in a wye system and will not be involved during the calibration process. Therefore, calibrating a delta-connected system requires at least one line-to-line transient on each of the two independent phases. As with the wye-connected network, any other multi-phase load that creates transients involving combinations of the independent phases is eliminated. By observing the fields created by the line-to-line calibration load applied on independent phases during each of these two serial tests, the algorithm can determine the current transformation and rotations of the independent phases. This result is post-processed using the method described in [17] to recover the current matrix and rotations for all three phases. Autonomous calibration was performed for a subpanel serving auxiliary shipboard loads. Single-phase equipment was cycled downstream of the subpanel to produce load transients; these included a heater and a fan that are located on different phases.

After calibrating the submeter, it monitored power continuously when the ship was in-port and also underway. The submetered panel serves loads that are typically used only during underway operation. An interval of the power data for both meters is shown in Fig. 12. The periods of high activity on the main panel correspond to daytime training exercises while the vessel is underway. These intervals match with increased power demand on the autonomously-calibrated subpanel. The total power consumption on the ship varies daily and depends on many factors, such as external temperature. Meanwhile, the subpanel pattern is fairly regular, corresponding to the use of key loads underway. The ship's radar system is among these loads and is always activated while at sea. The submeter provides a definitive pulsatile indication of radar operation, as illustrated in the figure Fig. 13. These pulses are more difficult to identify on the main panel, which experiences transients from other loads. The radar is vital to the ship's ability to navigate, and the submeter trace can provide important data both for confirming ship state and for diagnostic insights.

An additional non-contact meter was installed on the heating ventilation and air conditioning (HVAC) panel. This shipboard system is automatically controlled and always running. Consequently, loads cannot be manually switched on this subpanel to produce measurable transients. High-frequency sensor readings from this uncalibrated non-contact submeter were recorded while underway, in addition to the current measurements from the main panel. The HVAC system organically produced load transients during the course of its operation. An interval of data containing line-to-line transients on two different phases was used to autonomously calibrate the submeter. To verify the correctness of this result, the newly-determined current matrix and rotations were used to reconstruct the submeter currents form the sensor readings over a different time interval. This cross-validation is shown in Fig. 14 for more than an hour of underway operation. The load transients on the main panel and subpanel correspond in scale, phase isolation, and rotations. During both the calibration and

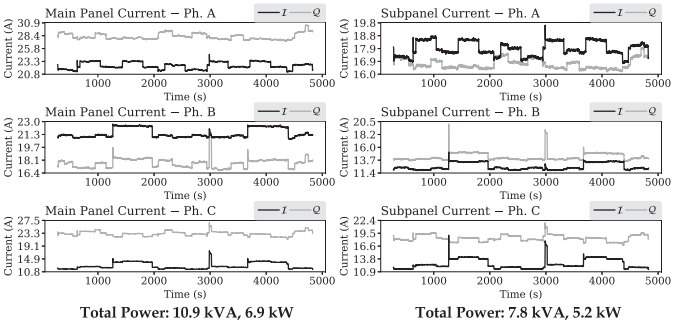

Fig. 14. The HVAC subpanel data (right) from an underway vessel demonstrates that this subsystem accounts for a majority of the energy usage. The currents on the main panel are shown for comparison (left).

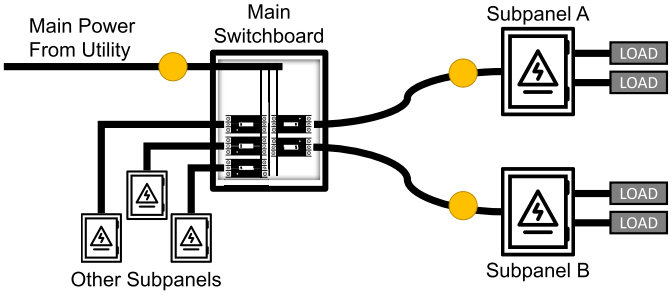

Fig. 15. Section of the radial power distribution network aboard the USCG Spencer. Subpanel A is located in a welding shop, and subpanel B serves receptacles throughout the ship. Yellow dots indicate the location of non-contact meters.

validation datasets, the HVAC system is responsible for greater than half the power consumption of the vessel. Metering of this subsystem was previously infeasible in the shipboard environment, and autonomous calibration enabled the impact of the HVAC system to be quantified for the first time.

C. Shipboard Application on a Coast Guard Vessel

Non-intrusive load monitors have been deployed aboard the U.S. Coast Guard Cutter (USCGC) Spencer for diagnosing failure of critical shipboard equipment [12]. This ship has a 440 volt delta-connected electrical system that is designed to sustain hundreds of amperes while underway. The main switchboard delivers power from the grid utility or onboard generators to dozens of subpanels through a radially-connected network. Autonomous calibration was employed on this vessel to calibrate non-contact meters on a main power feeder and on various subpanels.

First, a non-contact meter was installed on subpanel A and manually calibrated with a line-to-line test load sequentially applied on two independent phases. Another non-contact meter was installed on the forward shore-tie cable, which delivers power to the entire vessel from the utility. The topological relationship between the uncalibrated main meter and the calibrated submeter is shown in Fig. 15. During this *upstream* calibration, a 5 kW test load was cycled on the subpanel to provide load transients which both meters would measure. The autonomous calibration algorithm was applied to the ship's delta-connected network using the method described in the previous section. The currents of the main power feed were reconstructed from its meter's magnetic field measurements to

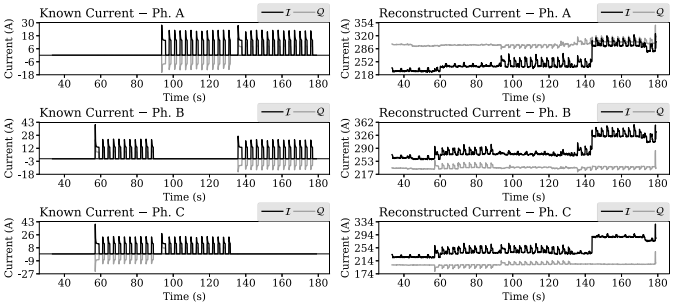

Fig. 16. The manually-calibrated meter on subpanel **A** acts as a current reference (left). The meter on the main power feed is autonomously calibrated to measure the subpanel's load transients in addition to other shipboard loads (right).

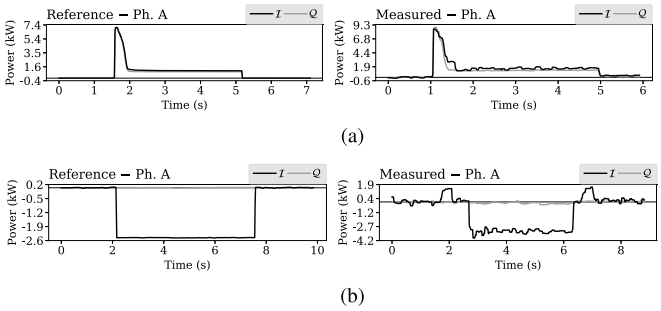

Fig. 17. Shipboard equipment measured with the autonomously-calibrated main meter (right) and a conventional submeter (left). The main power feed exhibits fluctuations caused by other existing loads. One phase is shown for each balanced 3-phase load. (a) Gray water pump. (b) Ship service diesel generator jacket water heater.

verify the resulting calibration. Figure 16 demonstrates that the test load produced identical transients at both meters. Several critical shipboard loads were also monitored with the autonomously-calibrated main meter, as shown in Fig. 17.

Conventional power meters have been used to monitor various subpanels on the ship. Non-contact sensing would greatly reduce the labor and electrical hazards associated with installing submeters in this environment. However, most shipboard panels provide no means to temporarily energize a test load for manual calibration. By using the known currents at the main meter, autonomous calibration can be used to install a non-contact meter on any subpanel that has at least two line-to-line loads on different phases. The autonomously-calibrated main meter from the previous experiment measures the current delivered to subpanel B, which also branches from the main switchboard in Fig. 15. A non-contact meter was installed on this subpanel, where a test load was cycled to produce measurable transients. The *downstream* calibration shown in Fig. 18 was able to accurately reconstruct the subpanel current transient. These experiments jointly demonstrate that an existing submeter can be used to autonomously calibrate a new subpanel by using a common upstream point in the system.

VI. Future Work

There are still many potential topics to explore in non-contact power monitoring calibration. The proposed algorithm

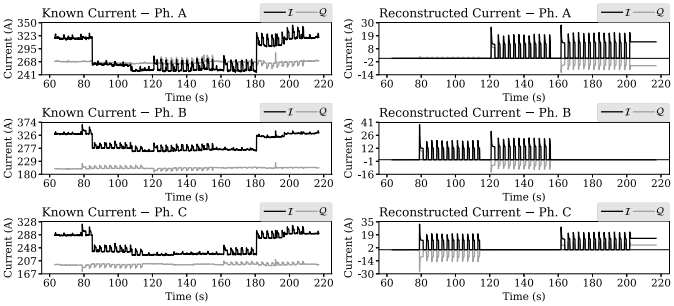

Fig. 18. The autonomously-calibrated meter on the main shore-tie provides known phase currents (left). Subpanel B is autonomously calibrated to recover the current transients of the test load (right).

requires single phase (or in the case of delta power systems, line-line) transients. One avenue for future work would be to examine relaxing the transient constraints to include multiphase loads or calibrating simply on steady state signals without requiring any transients. Additionally there is room for improvement in the voltage calibration. Many NILM algorithms only require the voltage angle so the current implementation is sufficient, but applications such as power quality and harmonic analysis could benefit from a robust multiphase voltage reconstruction. In a well regulated utility, the lack of transients in the electric field make calibration difficult. Poorly regulated utilities or micorgrids may provide a richer set of transients. They would also likely be the biggest beneficiary of a time domain voltage measurement.

VII. Conclusion

Mission-critical systems in industrial, commercial, and military environments may operate with little or no opportunity for scheduled downtime. Power system diagnostics that could be used for fault detection, diagnosis, and prognosis may be unavailable, therefore, unless originally installed with these systems. When retrofit or temporary power monitoring is desirable for energy score keeping, activity tracking, or diagnostic monitoring, non-contact power meters can acquire power information without the need to break a wire or make ohmic contact with a conductor.

This paper presents an autonomous calibration algorithm for non-contact power monitors. This algorithm makes it possible to install and calibrate non-contact power meters even when the electrical loads cannot be disturbed, altered, or added to for inclusion of a calibration load. Autonomous calibration permits power data from any other convenient meter at a site to provide a calibration reference for a new meter. This new meter can be installed upstream or downstream on a radial power distribution network for a "wide angle" or "zoomed in" view of a collection of loads.

This algorithm has been shown to be accurate and robust through a series of bench top experiments and real world deployments. Autonomously calibrated power monitors have enabled efficient submetering of US Navy YP vessels and expedited submeter deployment on a US Coast Guard Cutter.

Acknowledgment

The authors gratefully acknowledge the U.S. Naval Academy and the U.S. Coast Guard for granting access to their ships. They warmly acknowledge the assistance and advice of Daisy Green, Thomas Kane, and Dr. Peter Lindahl.

References

[1] I. Abubakar, S. N. Khalid, M. W. Mustafa, H. Shareef, and M. Mustapha, "An overview of Non-intrusive load monitoring methodologies," in *Proc. IEEE Conf. Energy Convers. (CENCON)*, Oct. 2015, pp. 54–59.

[2] J. S. Donnal and S. B. Leeb, "Noncontact power meter," *IEEE Sensors J.*, vol. 15, no. 2, pp. 1161–1169, Feb. 2015.

[3] J. M. Alcalá, J. Ureña, Á. Hernández, and D. Gualda, "Sustainable homecare monitoring system by sensing electricity data," *IEEE Sensors J.*, vol. 17, no. 23, pp. 7741–7749, Dec. 2017.

[4] A. Rahimpour, H. Qi, D. Fugate, and T. Kuruganti, "Non-intrusive load monitoring of HVAC components using signal unmixing," in *Proc. IEEE Global Conf. Signal Inf. Process. (GlobalSIP)*, Dec. 2015, pp. 1012–1016.

[5] W. J. Li, X. Tan, and D. H. K. Tsang, "Smart home energy management systems based on non-intrusive load monitoring," in *Proc. IEEE Int. Conf. Smart Grid Commun. (SmartGridComm)*, Nov. 2015, pp. 885–890.

[6] J. Gao, E. C. Kara, S. Giri, and M. Bergés, "A feasibility study of automated plug-load identification from high-frequency measurements," in *Proc. IEEE Global Conf. Signal Inf. Process. (GlobalSIP)*, Dec. 2015, pp. 220–224.

[7] H.-Y. Chen, Y.-C. Fan, C.-L. Lai, and H. Chen, "Identifying variable-power appliances in non-intrusive load monitoring systems," in *Proc. 10th Int. Conf. Innov. Mobile Internet Services Ubiquitous Comput. (IMIS)*, Jul. 2016, pp. 452–457.

[8] J. Paris *et al.*, "Scalability of non-intrusive load monitoring for shipboard applications," in *ASNE Day 2009*. Alexandria, VA, USA: American Society of Naval Engineers, 2009.

[9] L. Wu, P. A. A. F. Wouters, E. J. M. van Heesch, and E. F. Steennis, "On-site voltage measurement with capacitive sensors on high voltage systems," in *Proc. IEEE Trondheim PowerTech (POWERTECH)*, Jun. 2011, pp. 1–6.

[10] K. M. Tsang and W. L. Chan, "Dual capacitive sensors for non-contact AC voltage measurement," *Sens. Actuators A, Phys.*, vol. 167, no. 2, pp. 261–266, Jun. 2011.

[11] D. Lawrence, J. S. Donnal, S. Leeb, and Y. He, "Non-contact measurement of line voltage," *IEEE Sensors J.*, vol. 16, no. 24, pp. 8990–8997, Dec. 2016.

[12] P. Lindahl, G. Bredariol, J. Donnal, and S. Leeb, "Noncontact electrical system monitoring on a U.S. coast guard cutter," *IEEE Instrum. Meas. Mag.*, vol. 20, no. 4, pp. 11–20, Aug. 2017.

[13] J. Paris, J. S. Donnal, Z. Remscrim, S. B. Leeb, and S. R. Shaw, "The sinefit spectral envelope preprocessor," *IEEE Sensors J.*, vol. 14, no. 12, pp. 4385–4394, Dec. 2014.

[14] G. W. Hart, "Nonintrusive appliance load monitoring," *Proc. IEEE*, vol. 80, no. 12, pp. 1870–1891, Dec. 1992.

[15] R. Jain, R. Kasturi, and B. G. Schunck, *Machine Vision*, vol. 5. New York, NY, USA: McGraw-Hill, 1995.

[16] C. Fermüller and M. Pollefeys, "Edge detection," Tech. Rep., 2016.

[17] J. S. Donnal, P. Lindahl, D. Lawrence, R. Zachar, and S. Leeb, "Untangling non-contact power monitoring puzzles," *IEEE Sensors J.*, vol. 17, no. 11, pp. 3542–3550, Jun. 2017.

Andre Aboulian received the B.S. and M.Eng. degrees in electrical engineering and computer science from the Massachusetts Institute of Technology, in 2016 and 2018, respectively. His research interests include non-intrusive load monitoring, embedded electronics, and software systems.

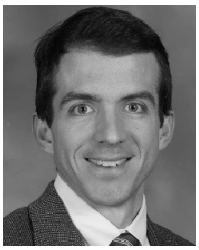

John S. Donnal received the B.S. degree in electrical engineering from Princeton University, Princeton, in 2007, and the M.S. and Ph.D. degrees in electrical engineering from the Massachusetts Institute of Technology, in 2013 and 2016, respectively. He is a Faculty Member of the U.S. Naval Academy in Weapons and Systems Engineering. His research interests include nonintrusive load monitoring synthesis, energy harvesting, and communications systems.

Steven B. Leeb received the Ph.D. degree from the Massachusetts Institute of Technology (MIT) in 1993. He has been a Faculty Member with the Department of Electrical Engineering and Computer Science, MIT, since 1993. He also holds a joint appointment with the Department of Mechanical Engineering, MIT. He is concerned with the development of signal processing algorithms for energy and real-time control applications.